Estimation of Mutual Coupling in Integrated Lens Arrays Using a Geometrical Optics-Based Technique With Bi-Directional Forward Ray-Tracing

Dabironezare, Shahab Oddin; Nair, Ashwita; Neto, Andrea; Llombart, Nuroa

DOI
10.1109/TAP.2024.3390998

Publication date
2024

Document Version
Final published version

Published in
IEEE Transactions on Antennas and Propagation

Estimation of Mutual Coupling in Integrated Lens Arrays Using a Geometrical Optics-Based Technique With Bi-Directional Forward Ray-Tracing

Shahab Oddin Dabironezare, *Member, IEEE*, Ashwita Nair, Andrea Neto, *Fellow, IEEE*, and Nuria Llombart, *Fellow, IEEE*

***Abstract*— The use of lens arrays in (sub)-millimeter sensing and communication applications will enable the development of integrated antenna front-ends with multiple independent beams as well as dynamic scanning capabilities. In applications such as MIMO communications, interferometric arrays, and Tx/Rx duplexing capabilities, a key parameter is the mutual coupling between the integrated antenna front-ends. In this work, we model such mutual coupling using a geometrical optics (GO) technique combined with bi-directional forward ray tracing. In this model, the mutual coupling is estimated by considering up to secondary reflections in lens array geometries. The proposed technique is then used to investigate the mutual coupling for low and high-density lens arrays as a function of feed locations. The accuracy of the model is also investigated in comparison to full wave simulations and measured data reaching a sufficient agreement to identify the regions within lens arrays with critical mutual coupling levels.**

***Index Terms*— Geometrical optics (GO), lens antenna, mutual coupling, submillimeter wave antennas.**

I. Introduction

FUTURE trends in imaging, communications, and sensing applications envision the exploitation of the (sub)-millimeter wave spectrum [1], [2], [3], [4], [5]. Systems operating at these wavelengths aim for directive antennas to meet the demanding requirements of these applications. More directive beams lead to a better angular resolution in imaging scenarios and a better signal-to-noise ratio in sensing and communication applications. Integrated lens arrays can be used to generate multiple directive beams and facilitate the front-end integration at these high frequencies. As a result, these types of arrays are emerging for several applications at (sub)-millimeter wavelengths [6], [7], [8], [9], [10], [11], [12], [13], [14], [15], [16], where the use of multiple planar antennas or small waveguides in combination with plastic or silicon dielectric lens arrays, see Fig. 1, is envisaged. Depending on the targeted application, the mutual coupling requirements in multibeam antenna systems can vary between −20 and −70 dB. For example, for communications [8], [17], [18], the mutual coupling between the different front-ends will impact the signal-to-noise and interference ratio of the link and therefore the potential capacity of the system. At these high frequencies, low-order modulation levels are being proposed [19] leading to mutual coupling requirements below −20 dB. Furthermore, in active sensing applications, such as frequency-modulated continuous-wave radars [20], the mutual coupling between transmitters and receivers can increase the phase noise, requiring isolation levels higher than 50 dB if the transmitting and receiving elements are placed below the same array. A more demanding example is imaging systems based on interferometric techniques for Earth observation [21] at millimeter waves that require extremely high feed isolations (∼70 dB) [22]. Other imaging instruments that could also benefit from assessing the mutual coupling levels are radiometric direct detector arrays, Day et al. [23] where the spilled-over radiation between lenses would impact the received noise.

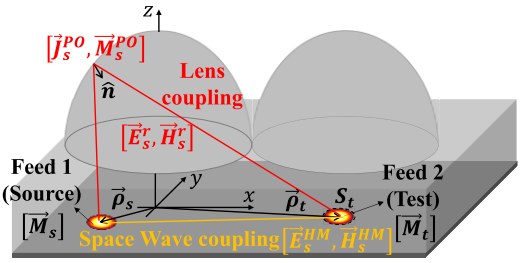

Fig. 1. Considered scenario for the evaluation of the mutual coupling in a lens array with the source and the test feeds located in the focal plane of the lenses at $\vec{\rho}_s$ and $\vec{\rho}_t$ positions, respectively.

To assess the potential of lens array configurations for these applications, the evaluation of mutual coupling between the integrated antenna front-ends is necessary. Previous works [24] and [25] have studied the effects of multiple reflections on the input impedance and mutual coupling of antennas below a single lens. In [25], a method based on geometrical optics (GO) and performing a reaction integral over the test feed was proposed. This test feed was placed at the mirror position with respect to the vertical axis of the lens and the location of the source feed where the lens's internal reflections are

Manuscript received 13 July 2023; revised 4 March 2024; accepted 5 April 2024. Date of publication 24 April 2024; date of current version 7 June 2024. *(Corresponding author: Shahab Oddin Dabironezare.)*

Shahab Oddin Dabironezare is with the Terahertz Sensing Group, Microelectronics Department, Delft University of Technology, 2628 CD Delft, The Netherlands, and also with the Technology Group, Netherlands Institute for Space Research (SRON), 2333 CA Leiden, The Netherlands (e-mail: s.o.dabironezare-1@tudelft.nl).

Ashwita Nair, Andrea Neto, and Nuria Llombart are with the Terahertz Sensing Group, Microelectronics Department, Delft University of Technology, 2628 CD Delft, The Netherlands.

Color versions of one or more figures in this article are available at https://doi.org/10.1109/TAP.2024.3390998.

Digital Object Identifier 10.1109/TAP.2024.3390998

the strongest. In this contribution, we extend these works to investigate the level of mutual coupling in lens arrays as a function of their geometry, arbitrary feed location, and material properties. To this end, we have developed a numerical technique based on an analysis in reception where the reaction integral is performed at the lens interface itself via the application of the reciprocity theorem. To evaluate the fields a bi-directional forward ray-tracing GO, similar to [26], is applied. The proposed technique shows fair agreement with full-wave simulations and provides a rapid evaluation compared to these simulations and standard forward GO/physical optics method.

The mutual coupling levels obtained by the proposed method are also compared to measured data obtained from a previously fabricated low-density lens antenna array. Using this technique, we investigated the main causes of the mutual coupling in lens arrays by separating this coupling into two main contributors: the direct space wave coming from the source, and the reflection contributions from the lens interface.

The article is structured as follows. Section II describes the proposed methodology to estimate the mutual coupling in lens arrays using GO and bi-directional ray tracing. Sections III and IV discuss the mutual coupling in example low and high-density lens arrays, respectively. The proposed technique is also validated in these sections using full-wave simulations. Section III also includes an experimental validation of the method. Concluding remarks are provided in Section V.

II. Methodology

The geometry under investigation is shown in Fig. 1. Two antenna feeds are located below an array of dielectric lenses. Feed 1 is the source antenna which radiates in the presence of the lens array while Feed 2 is the test antenna receiving the refracted fields from its surroundings. In this section, a description of the proposed methodology is presented.

A. Estimation of the Mutual Coupling in Reception

The mutual coupling between two antennas can be calculated in terms of the amount of power that the test feed receives from the total power radiated by the source feed. To evaluate this received power, one can resort to a reception formalism [8] by employing an equivalent Thévenin circuit. The induced open circuit voltage on the receiving test antenna, V_t^{oc}, can be evaluated by projecting the total fields radiated by the source antenna $[\vec{E}_s, \vec{H}_s]$ over the surface of the test antenna, S_t, enclosing its equivalent currents $[\vec{J}_t, \vec{M}_t]$ when operated in transmission

$$V_t^{\text{oc}} I_t^0 = \int\int_{S_t} \left[\vec{M}_t(\vec{\rho}_t) \cdot \vec{H}_s(\vec{\rho}_t) - \vec{J}_t(\vec{\rho}_t) \cdot \vec{E}_s(\vec{\rho}_t)\right] dS_t \quad (1)$$

where I_t^0 is the current that equivalently feeds the test antenna in transmission mode. In the case, where the surface S_t is located at a ground plane, thanks to the image theorem in reception, the equation reduces to [25]

$$V_t^{\text{oc}} I_t^0 = 2 \int \vec{M}_t(\vec{\rho}_t) \cdot \vec{H}_s(\vec{\rho}_t) dS_t. \quad (2)$$

Assuming impedance-matched antennas, the mutual coupling, S_{ts}, can be calculated as

$$|S_{\text{ts}}|^2 = \frac{P_t^l}{P_s^{\text{rad}}} = \frac{|V_t^{\text{oc}} I_t^0|^2}{16 P_t^{\text{rad}} P_s^{\text{rad}}} \quad (3)$$

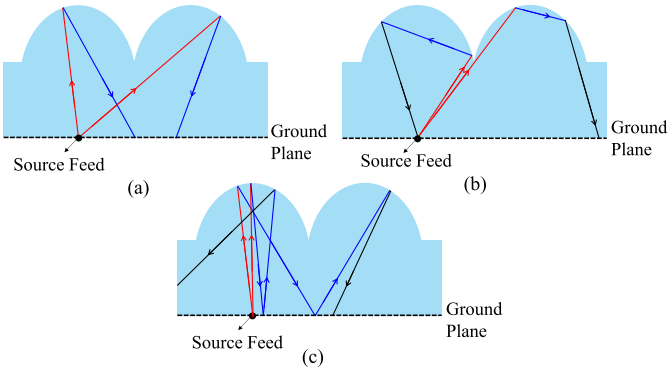

Fig. 2. Ray-tracing representation of the considered lens array contributions to the mutual coupling: (a) primary lens reflections, (b) secondary reflections within a lens element, and (c) secondary reflection via the ground plane. The red, blue, and black rays represent the incident, primary, and secondary reflected fields, respectively.

where P_t^l is the power delivered to the load of the receiving test antenna, and P_t^{rad} and P_s^{rad} are the total power radiated by the test and source antennas in the transmission mode, respectively. These radiated powers are evaluated in an infinite medium with the permittivity of the lens element.

The total magnetic field radiated by the source feed, $\vec{H}_s$, in the presence of an integrated lens can be decomposed into the field radiated by the feed into a homogenous medium, $\vec{H}_s^{\text{HM}}$, and the field refracted by the lens, $\vec{H}_s^r$, similar to the approach in [25]

$$\vec{H}_s \simeq \vec{H}_s^{\text{HM}} + \vec{H}_s^r. \quad (4)$$

The former is calculated in this section and leads to the space wave mutual coupling contribution, and the latter is calculated in Section II-B leading to an alteration to the coupling due to the presence of the lens.

The magnetic field radiated by the source feed into the homogenous medium, $\vec{H}_s^{\text{HM}}$, is evaluated using Green's function of an infinite homogenous medium with the same permittivity of the lens, $\overline{\overline{G}}^{\text{hm}}$, and the source feed's equivalent magnetic current, $\vec{M}_s$

$$\vec{H}_s^{\text{HM}}(\vec{r}) = 2 \int\int_{S_s} \overline{\overline{G}}^{\text{hm}}(\vec{r}, \vec{\rho}_s) \cdot \vec{M}_s(\vec{\rho}_s) dS_s \quad (5)$$

where S_s is the source feed's domain and factor two comes from the image theorem in transmission.

B. GO Propagation in the Lens Array

In this work, the contribution of the lens array to the mutual coupling is approximated via the use of physical optics (PO) equivalent currents. These currents are evaluated using a GO approach including up to the secondary reflections. Here, three types of reflection contributions are considered: 1) primary reflection of the source field at the lens array interface; 2) secondary reflection within a lens element; and 3) secondary reflection via the ground plane. These reflection contributions are shown in Fig. 2.

We can then approximate the magnetic field reflected by the lens when illuminated by the source feed as follows:

$$\vec{H}_s^r \simeq \vec{H}_{s1}^r + \vec{H}_{s2}^r \quad (6)$$

where $\vec{H}^r_{s1/2}$ is the primary/secondary reflected magnetic field by the lens surface [the secondary reflections include both cases represented in Fig. 2(b) and (c)]. This primary/secondary reflected magnetic field can be evaluated over the test feed domain by employing a standard PO integration

$$\vec{H}^r_s(\vec{r}) = 2\Bigg\{\int\int_{S_l} \overline{\overline{G}}^{\rm hm}(\vec{r},\vec{\rho}_s)\cdot\left[\vec{M}_{\rm s,r,1}+\vec{M}_{\rm s,r,2}\right]dS_l + \int\int_{S_l} \overline{\overline{G}}^{hj}(\vec{r},\vec{\rho}_s)\cdot\left[\vec{J}_{\rm s,r,1}+\vec{J}_{\rm s,r,2}\right]dS_l\Bigg\} \quad (7)$$

where $\overline{\overline{G}}^{\rm hm}$ and $\overline{\overline{G}}^{hj}$ are the dyadic Green's functions for the magnetic fields radiated by the equivalent magnetic and electric currents in an infinite homogenous medium, respectively; S_l is the lens array's surface, $[\vec{J}_{\rm s,r,1}, \vec{M}_{\rm s,r,1}]$ and $[\vec{J}_{\rm s,r,2}, \vec{M}_{\rm s,r,2}]$ are the equivalent currents associated with the primary and secondary reflections, respectively. It is worth noting that the factor two in (7) is due to the image theorem in transmission.

These equivalent currents can be calculated by employing a GO technique combined with forward ray tracing, similar to the one in [27]. Specifically, the far field of the source feed is propagated to the surface of the lens array, and referred to as the primary incident field, $[\vec{E}^{\rm GO}_{s,i1}, \vec{H}^{\rm GO}_{s,i1}]$. The primary transmitted and reflected GO fields are then calculated as

$$\vec{E}^{\rm GO}_{s,r1}(\vec{l}_1) = \overline{\overline{\Gamma}}(\vec{l}_1)\cdot\vec{E}^{\rm GO}_{s,i1}(\vec{l}_1) \quad (8a)$$
$$\vec{H}^{\rm GO}_{s,r1}(\vec{l}_1) = 1/\zeta_d\hat{k}_r\times\vec{E}^{\rm GO}_{s,r1}(\vec{l}_1) \quad (8b)$$
$$\vec{E}^{\rm GO}_{s,t1}(\vec{l}_1) = \overline{\overline{\tau}}(\vec{l}_1)\cdot\vec{E}^{\rm GO}_{s,i1}(\vec{l}_1) \quad (8c)$$
$$\vec{H}^{\rm GO}_{s,t1}(\vec{l}_1) = 1/\zeta_0\hat{k}_t\times\vec{E}^{\rm GO}_{s,t1}(\vec{l}_1) \quad (8d)$$

where $\vec{l}_1$ represents the intersection of the incident rays originating from the source feed's phase center with the lens surfaces as shown in Fig. 3; $\overline{\overline{\tau}} = \tau^{\perp}\hat{p}^{\perp}_t\hat{p}^{\perp}_i + \tau^{\parallel}\hat{p}^{\parallel}_t\hat{p}^{\parallel}_i$ and $\overline{\overline{\Gamma}} = \Gamma^{\perp}\hat{p}^{\perp}_r\hat{p}^{\perp}_i + \Gamma^{\parallel}\hat{p}^{\parallel}_r\hat{p}^{\parallel}_i$ are the transmission and reflection dyads, respectively; $\tau^{\perp}$ ($\Gamma^{\perp}$) and $\tau^{\parallel}$ ($\Gamma^{\parallel}$) are the perpendicular and parallel transmission (reflection) coefficients on the lens surfaces, respectively; $\hat{p}^{\perp/\parallel}_i$ represents the perpendicular and parallel polarization unit vectors of the incident field, while $\hat{p}^{\perp/\parallel}_t$ ($\hat{p}^{\perp/\parallel}_r$) are the ones of the transmitted (reflected) fields; ζ_0 and ζ_d are the characteristic impedance in air and lens dielectric mediums, respectively. The direction of the propagation of reflected and transmitted rays, $\hat{k}_r$ and $\hat{k}_t$, are calculated using the Snell's law.

The secondary ray tracing within a lens element [see Fig. 2(b)] is performed following the primary reflected rays that intersect again with the lens surface at locations $\vec{l}_2$, as shown in Fig. 3. The secondary incident fields are calculated by propagating the primary reflected fields using GO from the location $\vec{l}_1$ to $\vec{l}_2$

$$\vec{E}^{\rm GO}_{\rm s,i2}(\vec{l}_2) = \vec{E}^{\rm GO}_{\rm s,r1}(\vec{l}_1)\sqrt{\frac{\rho^1_{r1}\rho^2_{r1}}{(d_{r1}+\rho^1_{r1})(d_{r1}+\rho^2_{r1})}}e^{-jk_d d_{r1}} \quad (9)$$

where $d_{r1} = |\vec{l}_2 - \vec{l}_1|$ is the propagation distance of the primary reflected fields from the first to the second intersection with the lens surface; k_d is the propagation constant in the lens material. The radii of curvature of the primary reflected fields, ρ^1_{r1} and ρ^2_{r1}, are calculated using a formulation similar to the one reported in [28]. The primary reflected GO fields can pass one or both caustic points while propagating to the second intersection with the lens surface. These caustic points are located in the surroundings of the upper focus of the elliptical lens, F_1 in Fig. 3. The proper phase modification due to passing a caustic point is included in the propagation of the primary reflected fields [29]

$$\sqrt{\rho^j_{r1}/\left(d_{r1}+\rho^j_{r1}\right)} = \left|\sqrt{\rho^j_{r1}/\left(d_{r1}+\rho^j_{r1}\right)}\right|e^{j\pi/2} \quad \text{if } \rho^j_{r1}<0 \text{ and } d_{r1}>\left|\rho^j_{r1}\right|, \quad \text{for } j=1,2. \quad (10)$$

The secondary transmitted and reflected GO fields at the lens surfaces are then calculated as

$$\vec{E}^{\rm GO}_{s,r2}(\vec{l}_2) = \overline{\overline{\Gamma}}(\vec{l}_2)\cdot\vec{E}^{\rm GO}_{s,i2}(\vec{l}_2) \quad (11a)$$
$$\vec{H}^{\rm GO}_{s,r2}(\vec{l}_2) = 1/\zeta_d\hat{k}_r\times\vec{E}^{\rm GO}_{s,r2}(\vec{l}_2) \quad (11b)$$
$$\vec{E}^{\rm GO}_{s,t2}(\vec{l}_2) = \overline{\overline{\tau}}(\vec{l}_2)\cdot\vec{E}^{\rm GO}_{s,i2}(\vec{l}_2) \quad (11c)$$
$$\vec{H}^{\rm GO}_{s,t2}(\vec{l}_2) = 1/\zeta_0\hat{k}_t\times\vec{E}^{\rm GO}_{s,t2}(\vec{l}_2). \quad (11d)$$

The secondary ray tracing via the ground plane [see Fig. 2(c)] is performed following the primary reflected rays that intersect with the ground plane and then reflect again at the surface of a lens. These fields are estimated following similar steps to the ones for secondary reflections within a lens element.

Assuming the PO approximation of locally flat surfaces at each position on the lens, primary and secondary electric and magnetic equivalent currents are calculated over the lens array for incident, reflected, and transmitted GO fields and each lens surface

$$\vec{J}_{\rm s,i/r,1/2} \simeq \hat{n}\times\vec{H}^{\rm GO}_{\rm s,i/r,1/2} \quad (12a)$$
$$\vec{M}_{\rm s,i/r,1/2} \simeq \vec{E}^{\rm GO}_{\rm s,i/r,1/2}\times\hat{n} \quad (12b)$$
$$\vec{J}_{\rm s,t,1/2} \simeq -\hat{n}\times\vec{H}^{\rm GO}_{\rm s,t,1/2} \quad (12c)$$
$$\vec{M}_{\rm s,t,1/2} \simeq -\vec{E}^{\rm GO}_{\rm s,t,1/2}\times\hat{n} \quad (12d)$$

where $\hat{n}$ is the normal unit vector of the lens surface pointing toward the dielectric, $[\vec{E}^{\rm GO}_{s,i/r/t,1}, \vec{H}^{\rm GO}_{s,i/r/t,1}]$ are the electric and magnetic incident/reflected/transmitted GO fields evaluated over the lens surfaces for primary reflections while $[\vec{E}^{\rm GO}_{s,i/r/t,2}, \vec{H}^{\rm GO}_{s,i/r/t,2}]$ are the ones for the secondary reflections.

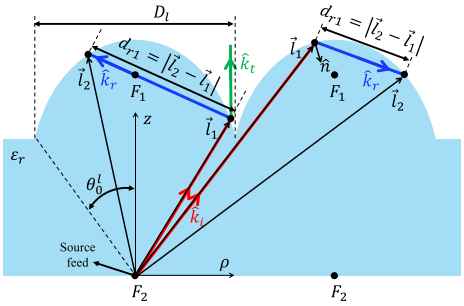

Fig. 3. Example illustration of the GO propagation for primary and secondary reflections in an elliptical lens array following a primary incident ray. The red, blue, and green colored lines represent the incident, reflection, and transmission rays, respectively.

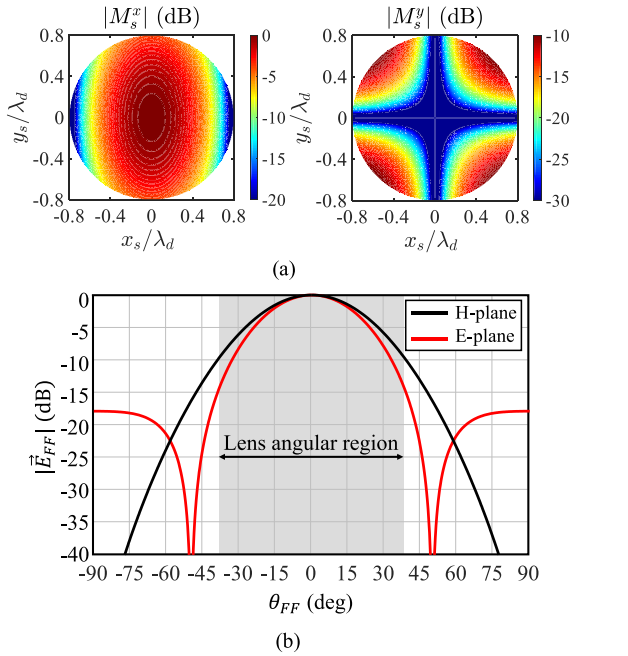

Fig. 4. (a) Normalized magnitude, in x- (left panel) and y-polarizations (right panel), of the equivalent magnetic current at the source feed's domain corresponding to a waveguide antenna with a diameter of $D_f = 1.6\lambda_d$, where λ_d is the wavelength in the plastic. (b) Normalized magnitude of the electric far-field of the same antenna in the semi-infinite plastic half-space. The angular region of the lens fed by this antenna, θ_0^l, is marked by the gray-colored region.

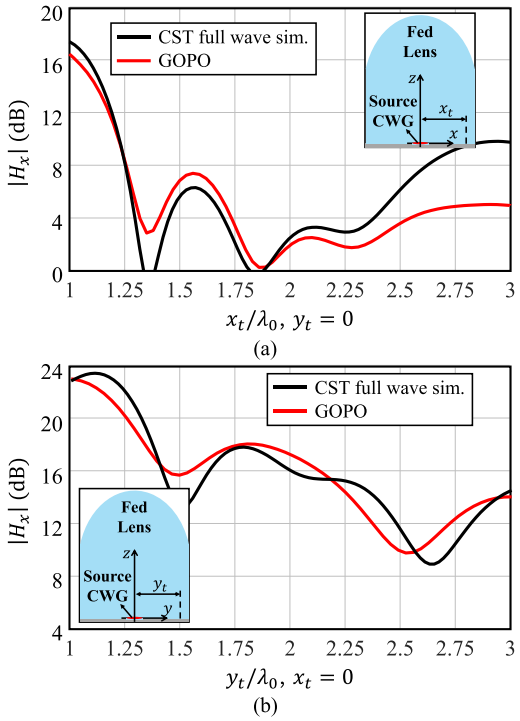

Fig. 5. Total magnetic field, including the space wave, primary, and secondary reflection contributions, calculated over the ground plane of the described lens antenna example case evaluated at (a) H-plane, (b) E-plane.

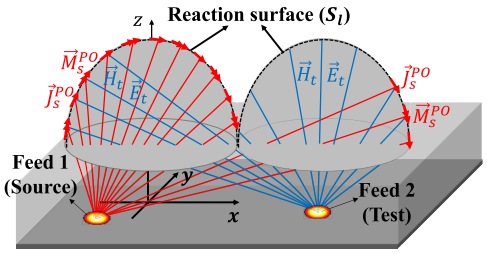

Fig. 6. Evaluation of the mutual coupling using a bi-directional ray-tracing approach.

Let us consider the case of a plastic lens element with relative permittivity of $\epsilon_r = 2.5$, diameter of $D_l = 6\lambda_0$, where λ_0 is the wavelength in free space and focal length to diameter ratio (f-number) of $f_\# = 0.81$, corresponding to a lens angular region of $\theta_0^l = 38°$. Here, we are considering only the fed lens (left side) in Fig. 3. In this example, a single-mode circular waveguide (CWG) filled with plastic with a diameter $D_f = 1.6\lambda_d$, where λ_d is the wavelength in plastic, is placed at the lower focus of the elliptical lens, F_2, where a ground plane is also present. The normalized magnitude of the equivalent magnetic current of this feed and its far-field are shown in Fig. 4(a) and (b), respectively. The chosen value for the magnitude of this current corresponds to radiating 0.5W of power by CWG in the far-field. In this example case, the single-mode CWG feed is y-polarized. The total magnetic field over the ground plane, (4), is validated against a CST Studio Suite [30] full wave simulation as shown in Fig. 5(a) and (b), for H- and E-plane, respectively. As it can be seen, the total magnetic field evaluated using the proposed method is in fair agreement with the one of CST, considering that CST simulation shows convergence difficulties for low amplitude field levels (the fields shown here are 20–40 dB below the maximum value at the feed location). We have also observed in the CST time domain simulations that the time of arrival of the pulses corresponding to secondary reflections is intertwined with the ones due to higher order edge reflections for positions close to the edge of the lens element. Moreover, we observed negligible effect from secondary reflections via the ground plane.

C. Reciprocity Method via Bi-Directional Ray-Tracing

The evaluation of the mutual coupling using the described procedure has an accuracy comparable to a standard PO approach and similar to [25]. However, this procedure is time-consuming due to two nested integrals: the one in (2) and the PO integration to calculate $\vec{H}_s^r$, (7). In order to speed up the calculations, the mutual coupling evaluation can be performed over the lens surface instead of the test feed surface (see Fig. 6) applying the reciprocity principle. As a result, a single integral is needed. This procedure, referred to as bi-directional ray-tracing, has been recently employed in other EM ray-tracing problems, such as [8] and [26].

To take advantage of this method, the open circuit voltage in (2) is expanded into two parts. A voltage generator representing the coupling of the two feeds in the homogenous medium of the lens (space wave coupling), and one that represents their coupling due to the presence of the lenses

$$V_{\text{oct}} I_{0\text{t}} = 2\int\int_{S_t} \vec{M}_t(\vec{\rho}_t)\cdot\vec{H}_s^{\text{HM}}(\vec{\rho}_t)dS_t + 2\int\int_{S_l}\left((\vec{M}_{s,r1}^{\text{PO}}+\vec{M}_{s,r2}^{\text{PO}})\cdot\vec{H}_t - (\vec{J}_{s,r1}^{\text{PO}}+\vec{J}_{s,r2}^{\text{PO}})\cdot\vec{E}_t\right)dS_l \quad (13)$$

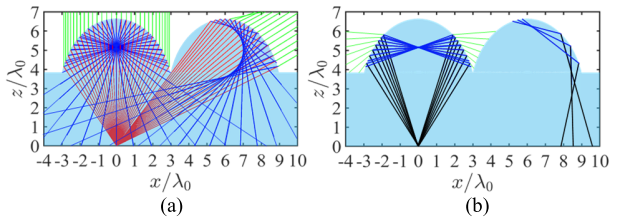

Fig. 7. Ray-tracing pictures corresponding to (a) primary and (b) secondary reflections in two neighboring plastic lenses along x-axis (H-plane). The red, blue, black, and green colored rays correspond to incidence, primary, secondary reflections, and transmission at the lens surfaces, respectively. A y-polarized CWG is located at the lower focus of the fed (left side) lens.

where $\vec{E}_t$ and $\vec{H}_t$ are the far fields radiated by the test feed evaluated over the lens surfaces, S_l. As will be shown in the next section for an example lens array case, the accuracy achieved using the bi-directional ray-tracing method is comparable to the PO approach while the computation time is five folds faster.

III. Mutual Coupling in Low-Density Lens Arrays

In this section, the described methodology in Section II is applied to an example case of low-density lens arrays. The estimated mutual coupling level using the proposed method is compared to full-wave simulations and measured data. For the former purpose, we consider the same feed and lens example as in Section II-B now in a lens array configuration. In this case, the source feed is placed at the lower focus of the left-side lens, referred to as the fed lens.

A. Evaluation of the GO Fields

The ray-tracing picture for the primary and secondary reflections of this example case is shown in Fig. 7(a) and (b), respectively. Here, a lens array with two elements is considered. The right-side lens is displaced in the x-axis (H-plane with respect to the considered mode of the CWG feeds). The red, blue, black, and green colored lines correspond to the incidence, primary, secondary reflections, and transmission rays, respectively. It is worth mentioning that the ray tracing associated with the secondary reflections inside a low-density lens occurs in clusters with overlapping areas. Therefore, a multisector GO interpolation technique has been applied to evaluate the secondary reflection fields as discussed in the Appendix.

The primary and secondary incident, transmitted, and reflected tangent GO electric fields evaluated over the lens surfaces are shown in Fig. 8(a)–(l). As can be seen in Fig. 8(c) and (f), the primary and secondary reflected fields on the fed lens have similar amplitude while the contribution from the former is spread over the focal plane of the lens array [see Fig. 7(a)] and the latter is concentrated around the focus of the fed lens [see Fig. 7(b)]. The primary reflections over the neighboring lens, Fig. 8(i), exhibits three distinct regions: shadow region due to the curvature of the lenses at the left side; total internal reflections occurring for the rays illuminating the center of the lens; while at the right side of the lens, fields are transmitted to air. These primary reflected fields are also spread over the shared focal plane of the lens elements leading to an increase in the mutual coupling below both lenses. The secondary reflected fields at the neighboring lens,

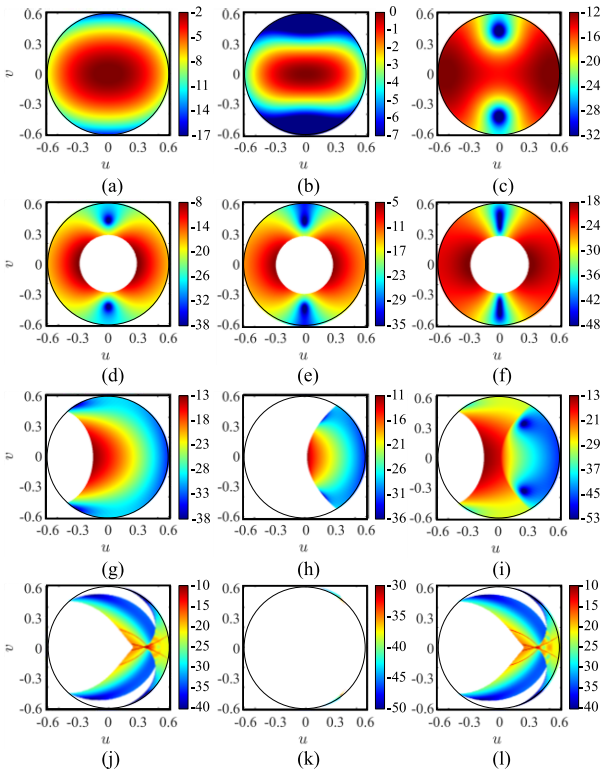

Fig. 8. Magnitude of the electric GO fields tangent to the lens surface corresponding to primary and secondary reflections in two neighboring plastic lenses along the x-axis (H-plane) in decibels for: primary (a) incidence, (b) transmission, (c) reflection and secondary (d) incidence, (e) transmission, (f) reflection over the fed lens; primary (g) incidence, (h) transmission, (i) reflection, and secondary (j) incidence, (k) transmission, and (l) reflection over the neighboring lens. The fields are normalized to their global maximum value. The black colored circles represent the angular region of the lenses.

Fig. 8(l), have a complex shape due to creation of ray clusters at different regions of the lens surface (see Appendix). These fields mostly contribute to an increase in mutual coupling for the feeds placed at the far-right side of the focal plane of the neighboring lens.

The ray-tracing picture for the contributions of the secondary reflection via the ground plane is shown in Fig. 9(a) and (b) using an imaged lens array for the sake of clarity. The tangent incident and reflected fields in this case are shown in Fig. 10(a)–(h). As can be seen, the secondary reflected GO fields via the ground plane are much lower in amplitude (at least 30 dB lower) with respect to the secondary reflections within a lens. This is due to the spread of the power over a large area while the rays are propagating between the lens surfaces and the ground plane; therefore, these reflected fields have a negligible contribution to the mutual coupling.

B. Evaluation of the Mutual Coupling Level

In Fig. 11, the mutual coupling between a test and a source feed is shown for the same plastic lens array of Fig. 7. Two cases are considered: 1) the test feed is displaced along x-axis (H-plane) and the center of the second lens is placed at $x_t = 6\lambda_0$, Fig. 11(a) and 2) the test feed is displaced along y-axis (E-plane) and the center of the second lens is placed at $y_t = 6\lambda_0$, Fig. 11(b). In these figures, the mutual coupling is provided as a function of the location of the test feed. The solid and patterned blue colored backgrounds in

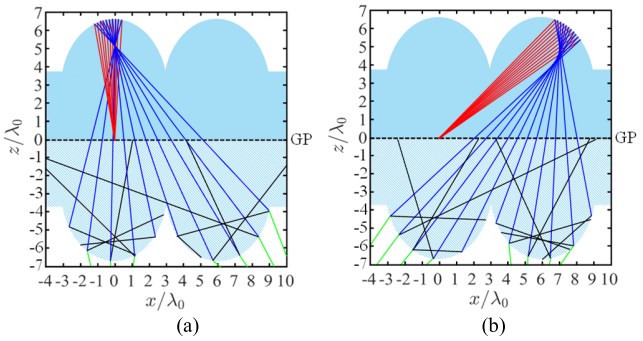

Fig. 9. Ray-tracing pictures corresponding to secondary reflections via the ground plane originating from (a) fed lens, and (b) neighboring lens when lens array is along the x-axis (H-plane). The red, blue, black, and green colored rays correspond to incidence, primary, secondary reflections, and transmission at the lens surfaces, respectively. A y-polarized CWG is located at the lower focus of the fed (left side) lens.

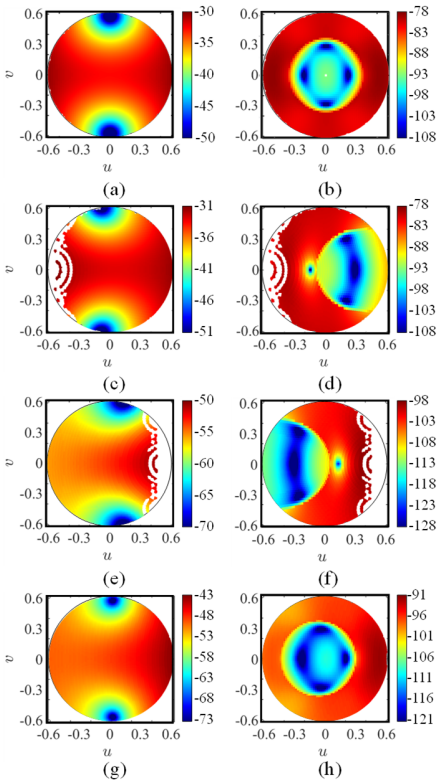

Fig. 10. Magnitude of the electric GO fields tangent to the lens surfaces corresponding to secondary reflections via the ground plane in decibels, for: secondary reflections originating from the fed lens evaluated over its surface for (a) incidence, and (b) reflection, and evaluated over the surface of the neighboring lens for (c) incidence, and (d) reflection; secondary reflections originating from the neighboring lens evaluated over the fed lens for (e) incidence, and (f) reflection; and evaluated over the neighboring lens for (g) incidence, and (h) reflection. The fields are normalized to the maximum value in Fig. 8. The black colored circles represent the angular region of the lenses.

the figures indicate the locations below the fed and second lenses, respectively. Fig. 11(a) also includes the results for a direct GOPO approach, (7), compared against the bi-direction ray-tracing approach, (13). The accuracy of both methods is comparable, while the second method is about fivefold faster.

Fig. 11 also includes full-wave mutual couplings evaluated using the time domain simulations in CST. For these full-wave simulations, two circular waveguide feeds are used. The

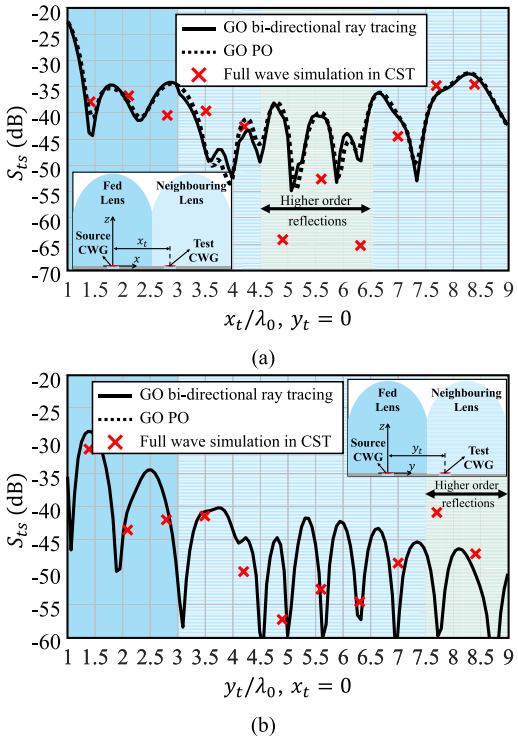

Fig. 11. Mutual coupling between two CWG feeds, when placed below the plastic lens array of Fig. 7, as a function of the displacement of the test feed. The source feed is located at the lower focus of the fed lens while the test feed is displaced in (a) H-plane and (b) E-plane. The insets indicate the location of the lenses and feed elements. Regions where higher-order reflections exist, as shown in Fig. 12, are also marked.

test feed is swept in location to recreate the cases shown in Fig. 11. One simulation is done per location and therefore the results are plotted with a set of red-colored crosses. As can be seen, the estimated mutual couplings using the proposed method are in good agreement with the ones of the full wave simulation despite only considering the primary and secondary reflections.

Higher-order reflections contribute to the discrepancies between the two methods at certain test locations. An example of such higher-order reflections is shown in the ray-tracing picture of Fig. 12 where the secondary transmissions from the fed lens propagate into the neighboring lens. Considering the distribution of the magnitude of the secondary transmitted fields over the fed lens surface [Fig. 8(e)], one can estimate which portion of these rays contribute more to E- and which to H-plane displacement cases, as marked in Fig. 12. In a first order estimation, it is expected that these higher order reflections contribute to the mutual coupling at test feed locations of $\sim 7.5\lambda_0$–$10\lambda_0$, and $\sim 4.5\lambda_0$–$6.5\lambda_0$, for E- and H-plane cases, respectively. This estimation is in line with the regions where discrepancies exist between the mutual coupling calculated using the full wave validation and the ones of the proposed method. These regions are also marked in Fig. 11. A field picture of the full wave simulation is shown in Fig. 13.

C. Experimental Validation

In this section, the proposed method is employed to evaluate the mutual coupling levels for a previously fabricated and measured low-density lens antenna array [12]. The mutual coupling between two neighboring feeds was reported in [12]

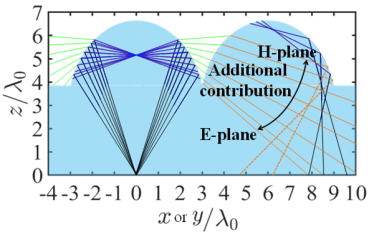

Fig. 12. Ray-tracing picture of the higher order reflections in the plastic lens array shown with solid and dashed orange-colored lines. The example case is the same as the one in Fig. 7(b) where the solid blue, black, and green colored lines correspond to the secondary incident, reflection, and transmission rays.

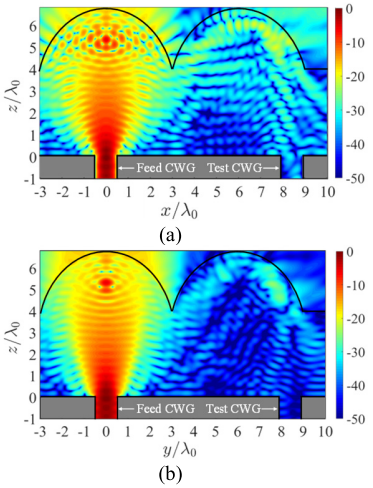

Fig. 13. Total electric field inside a linear plastic lens array obtained from the full wave simulation in CST for displacement in (a) H-plane and (b) E-plane.

as a function of frequency and provided in Fig. 14 as a reference to validate the proposed methodology in this article. The geometry is a linear (in E-plane) scanning phased array of plastic lenses, $\epsilon_r = 2.5$, with lens diameter of $D_l = 6\lambda_0$ (at 90 GHz) with subtended angle of $\theta_0^l = 36.5°$. In this prototype, circular waveguide feeds coupled to a resonant air cavity are used. These feeds present a frequency variation of the primary pattern in terms of amplitude and phase, see [12] and [14], that is modeled here via its far-field pattern radiated into an infinite medium with the same permittivity of the lens. The test and source feeds are located at the lower focus of their corresponding lenses which are displaced in the E-plane. Fig. 14 shows a comparison between these measured data and results obtained using the proposed GO based method. As it can be seen, the method agrees fairly well with the measurements.

D. Main Contributors to the Mutual Coupling

In this sub-section, the main contributors to the mutual coupling are studied in the described example case of a low-density lens array. In (13), three considered contributors are indicated: space wave, first, and second reflections. The mutual coupling contributions for H- and E-plane displacement cases are shown in Fig. 15(a) and (b), respectively. As can be seen, the dominant contributor to the mutual coupling differs in the case of the two main planes.

The far-field pattern of the circular waveguide feed is shown in Fig. 4(b) where the radiation toward 90° is significant in the E-plane with respect to the H-plane. As a result, it is

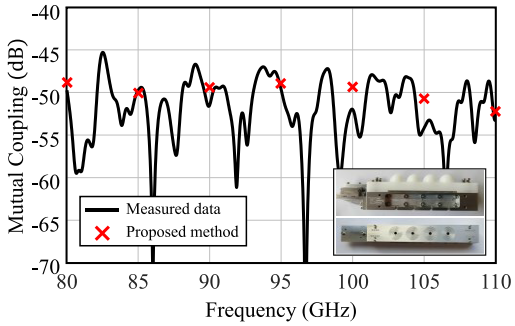

Fig. 14. Comparison between the measured mutual coupling between neighboring antenna feeds in a scanning linear phased array and results obtained by the proposed method as a function of frequency. The inset illustrates side and feed views of the prototype. Please refer to [12] for details on the prototype and measurement setup.

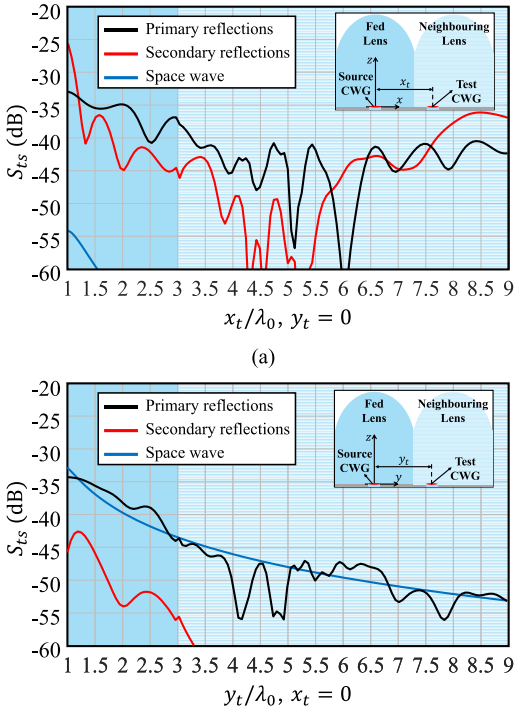

Fig. 15. Separated mutual coupling contributions between two CWG feeds, when placed below the plastic lens array of Fig. 7, as a function of the displacement of the test feed. The source feed is located at the lower focus of the fed lens while the test feed is displaced in (a) H-plane and (b) E-plane. The insets indicate the location of the lenses and feed elements.

expected that space wave coupling is more prominent in E-plane. The perpendicular reflection coefficient, corresponding to H-plane, leads to a larger portion of the power reflected with respect to parallel coefficient (E-plane). As a result, it is expected that the secondary reflections in H-plane contribute more significantly to the mutual coupling than the ones in E-plane. The ray-tracing picture in Fig. 7(b) also indicates that the contributions due to the second reflection are more significant around the focus point of the fed lens (at 0 position) and at locations toward the edge of the second lens (at $\sim 9\lambda_0$).

IV. Mutual Coupling in High Density Lens Arrays

In this section, the proposed methodology is applied to an example case of a high-density lens array. A similar case to

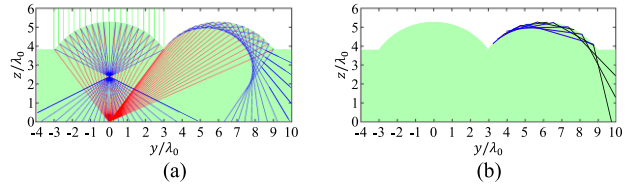

Fig. 16. Ray-tracing pictures corresponding to (a) primary and (b) secondary reflections in two neighboring silicon lenses displaced in the y-axis (E-plane). The red, blue, black, and green colored rays correspond to incidence, primary, secondary reflections, and transmission at the lens surfaces, respectively. A y-polarized CWG is located at the lower focus of the fed (left side) lens.

the one in Section III is considered with a relative permittivity of $\varepsilon_r = 11.9$. A set of waveguide feeds now filled with silicon and with a diameter of $D_f = 1.6\lambda_d$, where λ_d is the wavelength in silicon, are considered. The normalized magnitude of the equivalent magnetic current of these feeds and their far fields are the same as the ones shown in Fig. 4(a) and (b), respectively. The effect of the anti-reflection layer on the mutual coupling is also discussed.

The primary and secondary ray-tracing pictures for the silicon lens array case are shown in Fig. 16(a) and (b), respectively. The secondary reflections via the ground plane are considered which also led to negligible effect on the mutual coupling. The source feed is placed at the lower focus of the left side lens. It can be noted from this figure that no secondary reflections occur over the surface of the fed lens while no primary or secondary transmissions occur for the neighboring lens due to the critical angle. As a result, adding a matching layer over the lens elements would not reduce the reflections at the surface of the second lens. Due to the curvature of the dense lens, there is no need for applying segmentations as in the Appendix.

Full wave CST simulations are performed for the case of Fig. 16 to estimate the mutual coupling between two feeds. These simulations are performed for a lens array coated with a standard quarter wavelength matching layer. The results from CST are compared against the proposed method in Fig. 17(a) and (b), for H- and E-plane linear lens array cases, respectively. As can be seen, the agreement between the proposed method and full wave simulation is also reasonable. The main discrepancies in these results are located where the mutual coupling level is low at the surrounding of the fed lens in the H-plane and at the edge of the neighboring lens in the E-plane. The former is due to approaching the CST time domain accuracy level of -40 dB, while the latter is due to omitting the contribution of the creeping waves [31] by our proposed model which propagate along the surface of the neighboring lens in the secondary reflections.

In Fig. 17, the mutual coupling is also shown for lenses without a matching layer by dashed black curves. The presence of the matching layer mitigates the high mutual coupling below the fed lens; however, it does not have a similar effect on the surroundings of the second lens due to the total reflections occurring at its surface. From these curves, we observe that the mutual coupling level below the neighboring lens is higher than below the fed lens due to the total secondary reflections.

The execution time for calculating mutual coupling per test feed location for plastic and silicon lens arrays in CST was 42 and 102 min, respectively. The calculation of the proposed

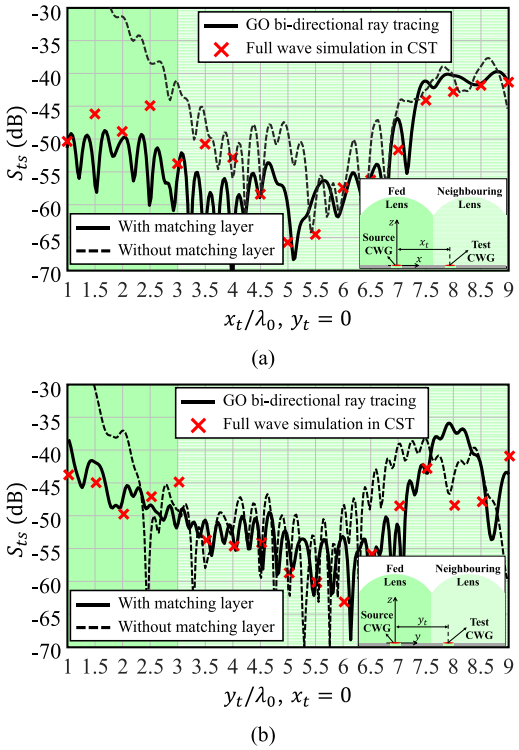

Fig. 17. Mutual coupling between two CWG feeds, when placed below the linear silicon lens array of Fig. 16, as a function of the displacement of the test feed. The source feed is located at the lower focus of the fed lens while the test feed is displaced in (a) H-plane and (b) E-plane. The insets indicate the location of the lenses and feed elements.

method elapsed in 3.2 and 1.2 min for plastic and silicon cases, respectively, using the same workstation.

V. Conclusion

In this contribution, a model is proposed to represent the impact of the mutual coupling in integrated lens antenna arrays. The mutual coupling is evaluated in reception mode where two feeds are considered: a source feed radiating in the presence of the lens array and a test feed receiving the scattered power from the source. Based on this representation, mutual coupling is estimated as the summation of three main contributions: space wave, primary, and secondary lens contributions. The former is evaluated by propagating the field radiated by the source feed antenna in an infinite medium while the lens contributions are evaluated via a bi-directional ray-tracing method combined with a GO technique. The method is applied to two arrays with low or high-density lens elements and circular waveguide feeds. The lens elements studied here have $6\lambda_0$ diameter, for which a GO/PO analysis is still valid. The variation of the mutual coupling and its three considered contributors are investigated in terms of polarization, presence of matching layer, and location of the test feeds.

The methodology is validated against full-wave simulations and measured data. The agreement with full-wave simulation is good in the regions where the field is dominated by the first and second-order reflections. The experimental validation against frequency also indicates the versatility of the method in providing a rapid and fairly accurate estimate of the mutual

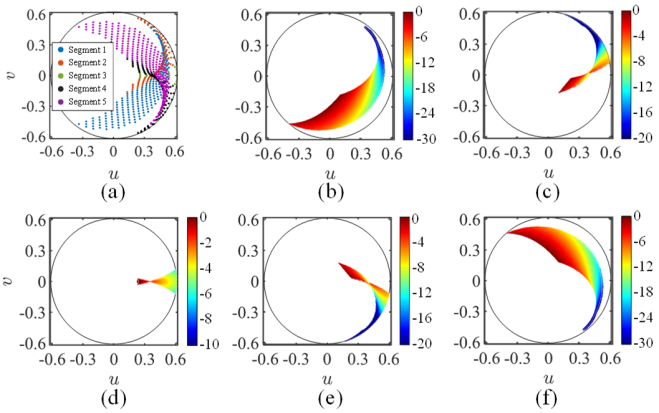

Fig. 18. (a) Intersection locations of the secondary incident rays, $\vec{l}_2$, with the neighboring lens (right side lens) for the same lens array case of Fig. 7. Different colors correspond to the five segments considered here. The magnitude of the tangent electric field for the secondary incident was evaluated over the neighboring lens for segment (b) 1, (c) 2, (d) 3, (e) 4, and (f) 5. The fields are normalized to their global maximum value. The black colored circles represent the angular region of the lens.

coupling levels in a realistic setting. The methodology provides only an accurate estimation of the mutual coupling in regions where the field is not dominated by higher-order reflections. These regions can be identified using ray tracing and are more pronounced around the edge of the lenses.

APPENDIX
MULTI-SEGMENT GO FIELD INTERPOLATION

In low-density elliptical lens arrays, due to the large curvature of the ellipsoidal surface, the secondary reflections within a lens element, Fig. 2(b), occur in clusters, i.e., they are concentrated at a certain region of the lens surface with coincidental ray-tracing locations and varying field values. In particular, the ray-tracing in the case of secondary reflections, the intersection locations $\vec{l}_2$ as indicated in Fig. 3 are scattered data points; therefore, the GO fields calculated at these locations are interpolated into a regular grid of data points in MATLAB. As a result, a single interpolation step inaccurately estimates the secondary reflected fields over the lens surface. In such cases, instead, the lens surface is separated into multiple segments. The secondary ray-tracing, GO propagation, and interpolation steps are performed separately for each of these segments. Afterward, taking advantage of the superposition principle, the interpolated GO fields of the segments are summed together.

The number of considered segments leads to a trade-off between the accuracy of the method and its execution time. In Fig. 18(a), this segmentation step is visualized for the neighboring (right-hand side) lens of the example case of Fig. 7(b). In this figure, different colored marks represent the intersection locations, $\vec{l}_2$, over the lens surface. Since these rays are emerging from different regions of the lens surface, they contain significantly different field values. The magnitude of the secondary incident fields at the surface of the neighboring lens is shown in Fig. 18(b)–(f) for each segment. The summation of these five field distributions is shown in Fig. 8(j).

ACKNOWLEDGMENT

The authors would like to thank Sjoerd Bosma, Nick van Rooijen, Maria Alonso-delpino, and Marco Spirito for providing the measured mutual coupling data of their scanning phased lens array prototype.

REFERENCES

[1] Y. J. Guo, M. Ansari, R. W. Ziolkowski, and N. J. G. Fonseca, "Quasi-optical multi-beam antenna technologies for B5G and 6G mmWave and THz networks: A review," *IEEE Open J. Antennas Propag.*, vol. 2, pp. 807–830, 2021.

[2] T. S. Rappaport et al., "Wireless communications and applications above 100 GHz: Opportunities and challenges for 6G and beyond," *IEEE Access*, vol. 7, pp. 78729–78757, 2019.

[3] R. Appleby and R. N. Anderton, "Millimeter-wave and submillimeter-wave imaging for security and surveillance," *Proc. IEEE*, vol. 95, no. 8, pp. 1683–1690, Aug. 2007.

[4] M. Köhler, J. Hasch, H. L. Blöcher, and L.-P. Schmidt, "Feasibility of automotive radar at frequencies beyond 100 GHz," *Int. J. Microw. Wireless Technol.*, vol. 5, no. 1, pp. 49–54, Feb. 2013.

[5] N. Llombart and S. O. Dabironezare, "Feasibility study of quasi-optical MIMO antennas for radiative near-field links," *IEEE Trans. Antennas Propag.*, vol. 70, no. 8, pp. 7073–7083, Aug. 2022.

[6] Z. Chen, C. N. Barati, J. Veihl, C. Shepard, and A. Sabharwal, "LensFD: Using lenses for improved Sub-6 GHz massive MIMO full-duplex," *IEEE Trans. Veh. Technol.*, vol. 72, no. 6, pp. 7517–7529, Jan. 2023.

[7] K. Konstantinidis et al., "Low-THz dielectric lens antenna with integrated waveguide feed," *IEEE Trans. THz Sci. Technol.*, vol. 7, no. 5, pp. 572–581, Sep. 2017.

[8] M. Arias Campo, D. Blanco, S. Bruni, A. Neto, and N. Llombart, "On the use of Fly's eye lenses with leaky-wave feeds for wideband communications," *IEEE Trans. Antennas Propag.*, vol. 68, no. 4, pp. 2480–2493, Apr. 2020.

[9] H. Jalili and O. Momeni, "A 0.46-THz 25-element scalable and wideband radiator array with optimized lens integration in 65-nm CMOS," *IEEE J. Solid-State Circuits*, vol. 55, no. 9, pp. 2387–2400, Sep. 2020.

[10] H. Zhang, S. Bosma, A. Neto, and N. Llombart, "A dual-polarized 27 dBi scanning lens phased array antenna for 5G point-to-point communications," *IEEE Trans. Antennas Propag.*, vol. 69, no. 9, pp. 5640–5652, Sep. 2021.

[11] M. Alonso-delPino, S. Bosma, C. Jung-Kubiak, G. Chattopadhyay, and N. Llombart, "Wideband multimode leaky-wave feed for scanning lens-phased array at submillimeter wavelengths," *IEEE Trans. THz Sci. Technol.*, vol. 11, no. 2, pp. 205–217, Mar. 2021.

[12] S. Bosma, N. Van Rooijen, M. Alonso-Delpino, M. Spirito, and N. Llombart, "First demonstration of dynamic high-gain beam steering with a scanning lens phased array," *IEEE J. Microw.*, vol. 2, no. 3, pp. 419–428, Jul. 2022.

[13] K. Trzebiatowski, W. Kalista, M. Rzymowski, L. Kulas, and K. Nyka, "Multibeam antenna for Ka-band CubeSat connectivity using 3-D printed lens and antenna array," *IEEE Antennas Wireless Propag. Lett.*, vol. 21, no. 11, pp. 2244–2248, Nov. 2022.

[14] S. Bosma, N. van Rooijen, M. Alonso-delPino, and N. Llombart, "A wideband leaky-wave lens antenna with annular corrugations in the ground plane," *IEEE Antennas Wireless Propag. Lett.*, vol. 21, pp. 1649–1653, 2022.

[15] H. Zhang, S. O. Dabironezare, J. J. A. Baselmans, and N. Llombart, "Focal plane array of shaped quartz lenses for wide field-of-view submillimeter imaging systems," *IEEE Trans. Antennas Propag.*, vol. 72, no. 2, pp. 1263–1274, Feb. 2024.

[16] J. J. A. Baselmans et al., "A kilo-pixel imaging system for future space based far-infrared observatories using microwave kinetic inductance detectors," *Astron. Astrophys.*, vol. 601, p. A89, May 2017.

[17] X. Chen, S. Zhang, and Q. Li, "A review of mutual coupling in MIMO systems," *IEEE Access*, vol. 6, pp. 24706–24719, 2018.

[18] I. Nadeem and D.-Y. Choi, "Study on mutual coupling reduction technique for MIMO antennas," *IEEE Access*, vol. 7, pp. 563–586, 2019.

[19] N. Llombart, D. Emer, M. Arias Campo, and E. McCune, "Fly's eye spherical antenna system for future tbps wireless communications," in *Proc. EuCAP*, 2017, pp. 1–4.

[20] K. B. Cooper, R. J. Dengler, N. Llombart, B. Thomas, G. Chattopadhyay, and P. H. Siegel, "THz imaging radar for standoff personnel screening," *IEEE Trans. THz Sci. Technol.*, vol. 1, no. 1, pp. 169–182, Sep. 2011.
[21] V. Kangas, S. D'Addio, M. Betto, H. Barre, M. Loiselet, and G. Mason, "Metop second generation microwave sounding and microwave imaging missions," in *Proc. EUMETSAT*, 2012, pp. 1–4.
[22] J. Christensen et al., "GAS: The geostationary atmospheric sounder," in *Proc. IEEE Int. Geosci. Remote Sens. Symp.*, Jul. 2007, pp. 223–226.
[23] P. K. Day, H. G. LeDuc, B. A. Mazin, A. Vayonakis, and J. Zmuidzinas, "A broadband superconducting detector suitable for use in large arrays," *Nature*, vol. 425, no. 6960, pp. 817–821, Oct. 2003.
[24] A. Neto, S. Maci, and P. J. I. de Maagt, "Reflections inside an elliptical dielectric lens antenna," *IEE Proc. Microw., Antennas Propag.*, vol. 145, no. 3, p. 243, 1998.
[25] A. Neto, D. Pasqualini, A. Toccafondi, and S. Maci, "Mutual coupling between slots printed at the back of elliptical dielectric lenses," *IEEE Trans. Antennas Propag.*, vol. 47, no. 10, pp. 1504–1507, Oct. 1999.
[26] M. M. Taygur and T. F. Eibert, "A ray-tracing algorithm based on the computation of (exact) ray paths with bidirectional ray-tracing," *IEEE Trans. Antennas Propag.*, vol. 68, no. 8, pp. 6277–6286, Aug. 2020.
[27] S. O. Dabironezare, G. Carluccio, A. Freni, A. Neto, and N. Llombart, "Coherent Fourier optics model for the synthesis of large format lens-based focal plane arrays," *IEEE Trans. Antennas Propag.*, vol. 69, no. 2, pp. 734–746, Feb. 2021.
[28] R. G. Kouyoumjian and P. H. Pathak, "A uniform geometrical theory of diffraction for an edge in a perfectly conducting surface," *Proc. IEEE*, vol. 62, no. 11, pp. 1448–1461, Nov. 1974.
[29] P. Pathak, "High frequency techniques for antenna analysis," *Proc. IEEE*, vol. 80, no. 1, pp. 44–65, Jan. 1992.
[30] *CST Microwave Studio, CST*. Accessed: Jun. 10, 2023. [Online]. Available: http://www.cst.com/
[31] D. Pasqualini and S. Maci, "High-frequency analysis of integrated dielectric lens antennas," *IEEE Trans. Antennas Propag.*, vol. 52, no. 3, pp. 840–847, Mar. 2004.

Shahab Oddin Dabironezare (Member, IEEE) was born in Mashhad, Iran. He received the M.Sc. and Ph.D. degrees in electrical engineering from Delft University of Technology (TU Delft), Delft, The Netherlands, in 2015 and 2020, respectively.

From 2020 to 2022, he was a Post-Doctoral Researcher with the Department of Microelectronics, Terahertz (THz) Sensing Group, TU Delft. He is currently an Assistant Professor at the THz Sensing Group, TU Delft, and an Instrument Scientist at the Netherlands Institute for Space Research (SRON), Leiden, The Netherlands. His research interests include wideband antennas at millimeter and submillimeter-wave applications, wide field-of-view imaging systems, quasi-optical systems, lens antennas, and absorber-based detector systems.

Ashwita Nair received the M.Sc. degree (cum laude) in electrical engineering from Delft University of Technology (TU Delft), Delft, The Netherlands, in 2021, where she is currently pursuing the Ph.D. degree with the Terahertz Sensing Group.

At TU Delft, her research focus is on the use of scanning lens arrays for automotive radars working at high frequency. During her master's, she worked on analyzing the impact of mutual coupling in integrated lens arrays. Her research interests include the analysis and design of planar antennas, integrated lens antenna arrays, and radar systems.

Andrea Neto (Fellow, IEEE) received the Laurea degree (summa cum laude) in electronic engineering from the University of Florence, Florence, Italy, in 1994, and the Ph.D. degree in electromagnetics from the University of Siena, Siena, Italy, in 2000. Part of his Ph.D. degree was developed at the European Space Agency Research and Technology Center, Noordwijk, The Netherlands.

He worked at the Antenna Section, European Space Agency Research and Technology Center, for over two years. From 2000 to 2001, he was a Post-Doctoral Researcher with California Institute of Technology, Pasadena, CA, USA, where he worked at the Submillimeter Wave Advanced Technology Group. From 2002 to January 2010, he was a Senior Antenna Scientist with TNO Defense, Security, and Safety, The Hague, The Netherlands. In February 2010, he became a Full Professor of applied electromagnetism at the Department of Electrical Engineering, Mathematics and Computer Science, Delft University of Technology, Delft, The Netherlands, where he formed and led the THz Sensing Group. His research interests include the analysis and design of antennas with an emphasis on arrays, dielectric lens antennas, wideband antennas, EBG structures, and THz antennas.

Dr. Neto is a member of the Technical Board of the European School of Antennas and an organizer of the course on antenna imaging techniques. He is also a member of the Steering Committee of the Network of Excellence NEW-FOCUS, dedicated to focusing techniques in millimeter and submillimeter-wave regimes. He was a recipient of the European Research Council Starting Grant to perform research on advanced antenna architectures for THz sensing systems in 2011, the H.A. Wheeler Award for the Best Applications Paper of 2008 in IEEE TRANSACTIONS ON ANTENNAS AND PROPAGATION, the Best Innovative Paper Prize of the 30th ESA Antenna Workshop in 2008, and the Best Antenna Theory Paper Prize of the European Conference on Antennas and Propagation (EuCAP) in 2010. He served as an Associate Editor for IEEE TRANSACTIONS ON ANTENNAS AND PROPAGATION from 2008 to 2013 and IEEE ANTENNAS AND WIRELESS PROPAGATION LETTERS from 2005 to 2013.

Nuria Llombart (Fellow, IEEE) received the master's degree in electrical engineering and the Ph.D. degree from the Polytechnic University of Valencia, Valencia, Spain, in 2002 and 2006, respectively.

During her master's degree studies, she spent one year at the Friedrich-Alexander University of Erlangen-Nuremberg, Erlangen, Germany, and worked at the Fraunhofer Institute for Integrated Circuits, Erlangen. From 2002 to 2007, she was with the Antenna Group, TNO Defense, Security and Safety Institute, The Hague, The Netherlands, working as a Ph.D. Student and afterward as a Researcher. From 2007 to 2010, she was a Post-Doctoral Fellow with California Institute of Technology, Pasadena, CA, USA, working with the Submillimeter Wave Advance Technology Group, Jet Propulsion Laboratory, Pasadena. She was a "Ramón y Cajal" Fellow with the Department of Optics, Complutense University of Madrid, Madrid, Spain, from 2010 to 2012. In September 2012, she joined the THz Sensing Group, Delft University of Technology, Delft, The Netherlands, where she has been a Full Professor, since February 2018. She has coauthored more than 150 journals and international conference contributions. Her research interests include the analysis and design of planar antennas, periodic structures, reflector antennas, lens antennas, and waveguide structures, with an emphasis on the THz range.

Dr. Llombart serves as a Board Member for the IRMMW-THz International Society. She was a recipient of the H. A. Wheeler Award for the Best Applications Paper of 2008 from IEEE TRANSACTIONS ON ANTENNAS AND PROPAGATION, the 2014 THz Science and Technology Best Paper Award from the IEEE Microwave Theory and Techniques Society, the 2014 IEEE Antenna and Propagation Society Lot Shafai Mid-Career Distinguished Achievement Award, the European Research Council Starting Grant in 2015, and several NASA awards.